

PAPER

# Single-shot grating-based phase-contrast imaging of a micrometer sample at a laser-driven x-ray backlighter source

To cite this article: B. Akstaller *et al* 2021 *JINST* **16** P06021

View the [article online](#) for updates and enhancements.

## You may also like

- [Anti-VEGFR2-conjugated PLGA microspheres as an x-ray phase contrast agent for assessing the VEGFR2 expression](#)  
Rongbiao Tang, Wei-Min Chai, Weihai Ying *et al*.
- [Image formation principles in coded-aperture based x-ray phase contrast imaging](#)  
A Olivo and R Speller
- [Experimental investigation of mouse kidney aging with SR PCI technology](#)  
P Yifeng, Z Zehua, D Guohao *et al*.



**IOP | ebooks™**

Bringing together innovative digital publishing with leading authors from the global scientific community.

Start exploring the collection—download the first chapter of every title for free.

# Single-shot grating-based phase-contrast imaging of a micrometer sample at a laser-driven x-ray backlighter source

B. Akstaller,<sup>a,\*</sup> S. Schreiner,<sup>a</sup> F. Hofmann,<sup>a</sup> P. Meyer,<sup>c</sup> P. Neumayer,<sup>b</sup> M. Schuster,<sup>a</sup> A. Wolf,<sup>a</sup> B. Zielbauer,<sup>b</sup> V. Ludwig,<sup>a</sup> T. Michel,<sup>a</sup> G. Anton<sup>a</sup> and S. Funk<sup>a</sup>

<sup>a</sup>Friedrich-Alexander Universität Erlangen-Nürnberg,  
Erwin-Rommel-Straße 1, 91058 Erlangen, Germany

<sup>b</sup>GSI Helmholtzzentrum für Schwerionenforschung GmbH,  
Planckstraße 1, 64291 Darmstadt, Germany

<sup>c</sup>Karlsruhe Institute of Technology Institute of Microstructure Technology,  
Hermann-von-Helmholtz-Platz 1, 76344 Eggenstein-Leopoldshafen, Germany

E-mail: [bernhard.akstaller@fau.de](mailto:bernhard.akstaller@fau.de)

**ABSTRACT:** A single-shot x-ray phase-contrast imaging technique with short exposure time allows to capture sharp images of fast dynamic processes despite low absorption contrast. We demonstrate the capabilities of a robust single-shot grating-based phase-contrast imaging setup at the Petawatt High-Energy Laser for Heavy Ion EXperiments (PHELIX) at the GSI Helmholtzzentrum für Schwerionenforschung GmbH. A static test sample was imaged at 47-fold magnification using a laser-driven high-energy x-ray backlighter source. The retrieved transmission and phase-contrast images yield reproducible results. The reconstructed differential phase-images are quantitatively explained. In addition to the phase-images, propagation signatures are found in the data and used for result verification. The obtained results demonstrate the capabilities of the grating setup which can be used to image microscopic dynamic processes in high-energy density plasma experiments at PHELIX or similar high-power laser facilities.

**KEYWORDS:** Inspection with x-rays; Plasma diagnostics - interferometry, spectroscopy and imaging; X-ray radiography and digital radiography (DR)

\*Corresponding author.

---

## Contents

|          |   |           |
|----------|---|-----------|
| <b>1</b> | <b>Introduction</b>                         | <b>1</b>  |
| <b>2</b> | <b>Materials and methods</b>                | <b>2</b>  |
| 2.1      | Data acquisition and image reconstruction   | 2         |
| 2.2      | Instrumentation                             | 3         |
| 2.3      | Concept of the quantitative evaluation      | 5         |
| <b>3</b> | <b>Results</b>                              | <b>6</b>  |
| 3.1      | Reconstruction of the differential phase    | 6         |
| 3.2      | Reconstruction of the transmission          | 7         |
| 3.3      | Check of the reproducibility of the results | 8         |
| <b>4</b> | <b>Conclusion and outlook</b>               | <b>10</b> |

---

## 1 Introduction

Phase-contrast imaging extends the attenuation image by additionally indicating the refractive properties of the object. There are several techniques that use phase-contrast in x-ray imaging. These are propagation based imaging [1–6], crystal interferometers [7, 8], edge-illumination [9, 10] or grating-based techniques at synchrotrons [11–13] or common low-brilliance sources [14].

Grating-based phase-contrast has been largely developed in the fields of medical imaging [14, 15] and non-destructive testing [16–19]. A further application is to image laser-produced plasmas at x-ray laser facilities [20]. Phase-contrast imaging of test objects in x-ray backlighter experiments has been conducted with a three-grating Talbot-Lau setup at high-power laser facilities [21, 22] like CELIA [23] or Omega EP [24]. Phase-contrast imaging at the PHELIX facility was demonstrated with propagation based phase-contrast images of static samples and a plasma [25, 26].

In this paper, we present images of static test objects at high magnification and with short exposure times, demonstrating the feasibility of phase-contrast imaging with a robust two-grating setup at PHELIX. The 47-fold magnification allows to image a micron sized sample. Furthermore, using only two instead of three gratings increases the photon-flux at the detector and improves the flexibility of the setup. Phase and attenuation images were obtained with a robust two-grating phase-contrast setup that was aligned using a fast alignment method [27]. In-line signatures were identified in the transmission images and evaluated separately to confirm the findings from the phase-reconstructions. The measurements are compared to model calculations. Although the x-ray spectrum is not known precisely, which is challenging for the quantitative evaluation of the images, good agreement was found between the experiment and the calculated models. This demonstrates the feasibility of single-shot grating-based phase-contrast imaging with high magnification using a backlighter source at the PHELIX facility.

The PHELIX high-power laser is capable of delivering two intense laser pulses with a delay time of up to 10 ns in one shot. This, and the short exposure time enabled by the backlighter x-ray source, allow to image laser plasmas in high-energy density pump-probe experiments at this facility [25]. This type of experiment is interesting for inertial confinement fusion or laboratory-astronautics [28].

## 2 Materials and methods

### 2.1 Data acquisition and image reconstruction

The presented data comprises three images taken of static test objects during shots A, B and C, while a fourth shot without any object present provides the reference image. The object is a piece of polyimide foil that extends 1 mm in line-of-sight but is only 25  $\mu\text{m}$  thick in lateral direction (horizontal direction in figure 1). Together with the backlighter wire, the sample is replaced by an identical one for each measurement. The laser pulse energy and the exact shape and position of the laser spot are not perfectly reproducible from shot to shot, but were kept as constant as possible.

The reference image and the object image of shot A are presented in figure 1. The thin polyimide foil appears as a dark stripe in the central region of the object image. Both images show horizontal moiré stripes. To quantify the image noise, the standard deviation in the background of the raw images can be determined along the moiré stripes. It lies around 6% of the background mean intensity.

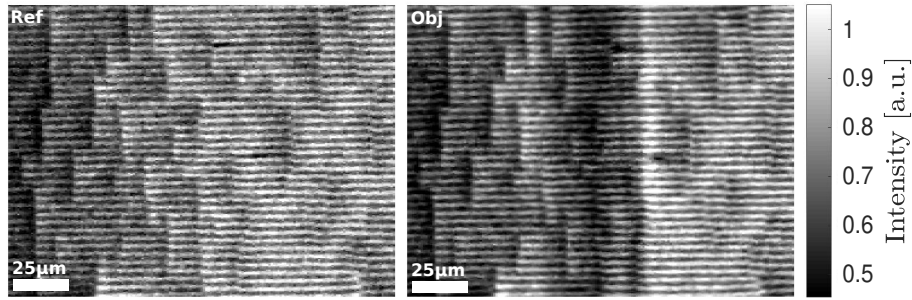


**Figure 1.** Raw images of the reference shot on the left (Ref) and of object shot A on the right (Obj). Both images exhibit the same horizontally striped moiré pattern. The vertical lines that appear mainly in the left halves of the images are artifacts that stem from scratches in the G2 grating. In the object image, the 25  $\mu\text{m}$  wide polyimide foil is visible as a vertical stripe in the centre. The mean fringe pattern visibility on the right side of the object is 16 %. The greyscale corresponds to the normalised intensity.

In grating-based phase-contrast imaging, the self-image of an x-ray transmission grating is analysed to calculate the differential phase-shift imprinted on the x-rays by an object. When illuminated coherently, a grating G1 produces a self-image at the Talbot distance  $d_T$  and further intermediate Talbot images at fractional Talbot distances  $d_F$  [29, 30]. The Talbot distance depends on the G1 grating period  $p_1$ , the wavelength  $\lambda$  of the radiation and the type of grating. For the presented setup, a  $\pi$ -phase shifting grating with  $p_1 = 10 \mu\text{m}$  was used as G1. In the geometries typically used in single-shot grating-based phase-contrast, the fringes of the G1 self-image cannot be resolved directly by the (large area) detector, which is why an additional absorption grating G2 is placed at a fractional Talbot distance between G1 and the detector [12]. This causes moiré stripes

to appear in the detector plane, large enough to be resolved directly by the detector. The moiré stripes carry the same phase information as the G1 self-image, albeit with a lower resolution. In the raw images (figure 1), these fringes can be seen as horizontal stripes. Their orientation and periodicity can be tuned by adjusting the position of the gratings relative to each other, to the x-ray source and to the detector. Our setup was adjusted to yield a moiré pattern with a periodicity of about  $345\text{ }\mu\text{m}$  in the detector plane. The mean fringe visibility is 16 % with a standard deviation of 6 % throughout the field of view. The visibility  $V$  is defined by the maximum ( $I_{\text{max}}$ ) and minimum intensity  $I_{\text{min}}$  values of the fringe pattern, as

$$V = \frac{I_{\text{max}} - I_{\text{min}}}{I_{\text{max}} + I_{\text{min}}}.$$

The fringe pattern can be separated from the object information in Fourier space [31], resulting in three image modalities. The first modality is referred to as the differential phase-contrast. A diffractive object placed in the beam path can locally distort the moiré pattern in the detector plane. The lateral movement of the fringes corresponds directly to the differential phase-shift of the wave that was imprinted by the object. The second modality is referred to as the transmission image. Here, the fringes are removed by the reconstruction so that the image is equivalent to a standard radiography. The third modality is the dark-field image which corresponds to small angle scattering in the sample [16, 32]. Since no dark-field signal was found in our data, this modality will not be discussed further. After reconstructing the transmission and phase-images, the respective reference is used to separate the object information from the background of the image.

## 2.2 Instrumentation

The experiment was conducted at the Petawatt High-Energy Laser for Heavy Ion EXperiments (PHELIX) [33]. To produce the x-rays, a  $5\text{ }\mu\text{m}$  tungsten backlighter wire was irradiated by a 700 fs infrared laser pulse with an energy of 25 J to 30 J. The focused high-energy laser pulse destroys the wire in an explosion, so that a broad spectrum of hard x-rays is emitted. The generated spectrum is not exactly reproducible between two shots due to laser intensity variations and small differences of the effective focus spot on the backlighter wire. We estimate the position stability of the source to be better than  $20\text{ }\mu\text{m}$  from shot-to-shot. The vertical x-ray source size is limited by the wire diameter of  $5\text{ }\mu\text{m}$ . The horizontal size is about  $10\text{ }\mu\text{m}$  to  $20\text{ }\mu\text{m}$  depending on the laser intensity [34]. Thus, the thin backlighter wire provides x-rays with sufficient spatial coherence, so that a good moiré visibility can be achieved without using a source grating [14, 27].

Fuji BAS type SR imaging plates with a spatial resolution of  $109\text{ }\mu\text{m}$  [35] were used as x-ray detectors. The plates were protected by an  $8\text{ }\mu\text{m}$  thin aluminium layer to shield them from visible light. Readout was done using a scanner with a  $50\text{ }\mu\text{m}$  raster, small enough so as to not reduce the resolution of the imaging plates any further. After scanning, the obtained images are cropped to the relevant region of interest and then matched with help of markers on the G2.

The imaging setup is presented in figure 2. It is designed with high image magnification to achieve a resolution of a few microns in the object plane. The design distance between source and object is 20 mm while the distance between the source and the detector is 943 mm, yielding a magnification of approximately 47. The gratings G1 and G2 are 217 mm and 75 mm away from the detector. Both gratings are manufactured by the Institute of Micro Structure Technology (IMT)

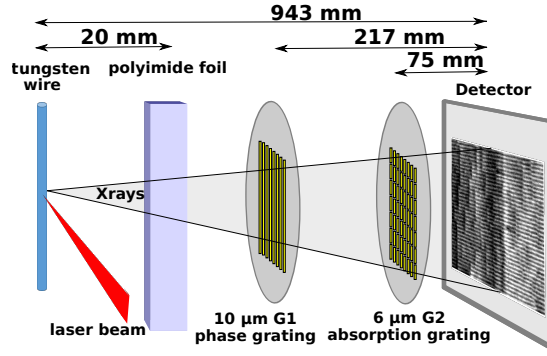


**Figure 2.** Schematic of the imaging setup (not to scale). The laser-powered, 5  $\mu\text{m}$  thick tungsten backlighter wire produces x-rays which are used to image the polyimide foil. The gratings G1 and G2 are mounted in a rigid portable setup. The image of the foil is projected onto the imaging plate detector.

at the Karlsruhe Institute of Technology (KIT) with the deep x-ray LIGA process [36, 37]. The substrate used for both gratings is a 500  $\mu\text{m}$  thick polyimide 4 inch wafer. With a G2 grating period of 6  $\mu\text{m}$ , the structure gold height is around 150  $\mu\text{m}$ . This height provides sufficient absorption for the high energies that are present in the broad x-ray spectrum, while the fine period increases the overall phase-sensitivity of the setup.

For moiré imaging, the gratings must be aligned to each other and to the x-ray source with a very high precision. The alignment of the setup components is usually done in an iterative procedure of adjusting the setup and taking test images. This is not feasible here, since the PHELIX main amplifier requires a 90 minutes cool-down time after every shot. A fast alignment method for grating-based imaging systems [27] was required. For this method, the setup must be pre-aligned in the home lab. Then, slightly misaligned states of the moiré pattern are recorded and charted on a look-up table. With that, the setup is transported to the backlighter experiment and carefully installed with respect to the x-ray source while keeping the specified distance between the gratings and the source. The first backlighter shot is performed with a slightly misaligned setup. However, comparing the resulting image with the images charted on the look-up table yields the instruction on how to blindly correct this misalignment [27]. The result is a well-aligned setup for the second shot.

The x-ray spectrum has a considerable influence on the performance of a grating-based imaging setup. For laser-induced x-ray generation, a broad energy spectrum is expected. The spectrum was previously investigated in comparable backlighter experiments at PHELIX. Borm et al. [34] investigated the energy range from 20 keV to 70 keV and found intensity variations in the range of 20 %. Further, they determined the spectrum with a Maxwellian distribution at temperatures varying between 30 keV and 100 keV. However, the model does not regard emission lines. Further, the moiré visibility and the sensitivity of our imaging detector are energy-dependent (see figure 3 or [35]), so it is difficult to simulate an effective spectrum. Seifert et al. [38] determined the weighted mean energy of the imaging system experimentally to lie between 11 keV and 12 keV using the same x-ray source and detector. Instead of gratings the setup had an acrylic window in the beam path with absorption properties comparable to our grating substrates. So, we optimised our imaging setup based on the results of Seifert et al., to yield a good moiré visibility in the energy range between 11 keV and 12 keV. The expected visibility for our setup is plotted, scaled by the



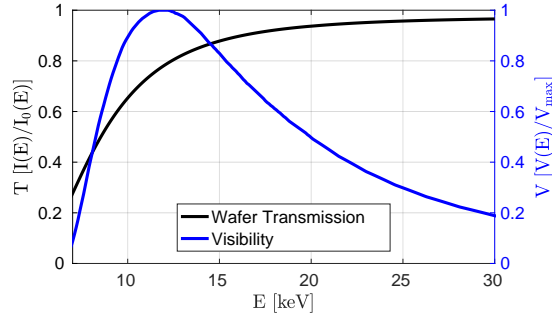


**Figure 3.** Model calculation of the wafer transmission  $T$  and simulation of the moiré visibility  $V$ . The transmission through the two  $500\text{ }\mu\text{m}$  wafers (black line) is plotted in the energy range from 6 keV to 30 keV. The transmitted intensity  $I$  is scaled relative to the incoming intensity  $I_0$ . The simulated visibility is plotted for the same energy range. Here, the y-axis is scaled relative to the maximum value  $V_{\text{max}}$  for the visibility that is found at an energy of 12 keV.

maximum value of the visibility  $V_{\text{max}}$  at 12 keV, in the energy range between 7 keV and 30 keV in figure 3. It is given relative to the maximum value of the visibility  $V_{\text{max}}$ , which lies at 12 keV. The x-ray transmission of the grating wafers is plotted alongside to show that the transmission through the gratings is high at the energies where the setup yields the highest visibility. The lower energies are largely absorbed by the wafers. Further, the higher energies have a reduced visibility, so their impact on the moiré fringes is weaker. The moiré visibility affects the grating-based phase reconstruction, but not the transmission image. Thus, we expect that the higher energies should contribute less to the phase-image than to the transmission image. This could affect the effective mean energy for the two image modalities. However, without specific knowledge about the shape of the backlighter spectrum, this is rather a speculation about the tendencies in the spectra of the radiation that forms the different image modalities.

### 2.3 Concept of the quantitative evaluation

For a quantitative evaluation of the retrieved images, the expected phase-contrast and transmission signatures are calculated using a simple object model. Then they are compared to the actual measurement data.

The absorption and the phase-shift of x-rays in a medium are described by the complex refractive index  $n = 1 - \delta + i\beta$  with the imaginary part  $\beta$  and the decrement  $\delta$ . The energy-dependent values of both parameters for polyimide can be found in [39]. We calculate the modulation of the x-ray wave by the object using the projection approximation. The transmitted intensity follows the Beer-Lambert law, while the phase profile induced by the object can be calculated with  $\Phi(x, y) = \delta k z(x, y)$ , where  $z(x, y)$  is the projected object thickness profile and  $k$  the wavenumber [40]. The modulation of the phase can be detected by the grating-based phase-contrast imaging setup with a certain phase-sensitivity. The phase-sensitivity increases for a finer G2 grating period  $p_2$  and a larger distance  $d_{G1G2}$  between G1 and G2. The differential phase-contrast DPC can be calculated for given object properties and geometries with [13]

$$\text{DPC} = \frac{1}{M_{G1}} \frac{\lambda d_{g1g2}}{p_2} \partial_x \Phi(x, y), \quad (2.1)$$

where  $\partial_x$  is the partial differentiation in x-direction (horizontal image axis).  $M_{G1}$  is the geometric magnification of the object into the G1 plane. The factor  $1/M_{G1}$  in the equation accounts for the reduction of the phase-sensitivity with increasing distance between the object and the phase grating [41]. Hence, there is a trade-off between image magnification and phase-sensitivity. The calculation of the phase-image is performed using geometric considerations. But the same model applied to the transmission data gives large discrepancies with the experimental data, so the diffraction of the wave during the propagation from the object to the detector plane is simulated with Fresnel diffraction, following the description in [40].

The thin foil used as test object can be approximated as a cuboid with a very high aspect ratio. The foil is slightly tilted (around the vertical image axis) in such a way that it is seen slightly from the side. Thus, the projected thickness profile  $z(x, y)$  of the foil has a trapezoidal shape. Due to the limited precision of the mounting procedure, the tilt angle changes from shot to shot. Still, this allows to model the whole experiment with a simple approximation for the object geometry. Further, the symmetric shape of the test object in the vertical direction allows to reduce the calculation to only one horizontal line segment of the foil.

To add image blur to the calculated trapezoidal signal, a convolution with a Gaussian kernel is applied. For both the transmission and the phase-images, the kernel models blurring that stems from the  $5\text{ }\mu\text{m}$  source width and the  $109\text{ }\mu\text{m}$  point spread function of the imaging plates. With this, the calculated data can be better compared to the measurement data.

Each calculation of the image signatures is repeated for multiple energies. The energy that best reproduces the measurement data is assumed to be the weighed mean energy of the imaging system (compare [38]). This procedure neglects that spectral contributions at higher or lower energies can distort the signals due to non-linear absorption- or phase-effects. To illustrate the impact of the spectral influences, the calculations are plotted with an uncertainty band that represents the signal in a range of  $\pm 1\text{ keV}$  around the determined energy. A more precise evaluation was not considered due to the limited reproducibility of the backlighter x-ray spectrum.

### 3 Results

#### 3.1 Reconstruction of the differential phase

The differential phase-contrast image taken with shot A is presented in the figure 4 inset. The signal of the foil is visible as the dark-and-bright stripe in the centre of the image. In the background to the right of the object, the image noise can be observed. The standard deviation  $\sigma_{\text{DPC}}$  of the phase-signal fluctuation in the background region is 0.3 rad. For the quantitative evaluation of the image, 80 lines are averaged over the region of interest to obtain a lineplot. This measurement data is shown as dots in the plot in figure 4. The standard deviation in the background of the lineplot is 0.1 rad. The signal amplitude of the object is roughly 0.6 rad from minus-peak to plus-peak, which is twice the image standard deviation and 6 times the standard deviation in the line-averaged data.

The data is overlaid with the calculated phase-signal (solid line). The plotted  $\pm 1\text{ keV}$ -band does not account for image noise, but only demonstrates the influence of the 1 keV error band in the effective mean energy on the calculated signals. The negative-positive behaviour of the curves is typical for a differential phase. Since  $\delta$  is typically smaller than 1 in the x-ray regime, a negative



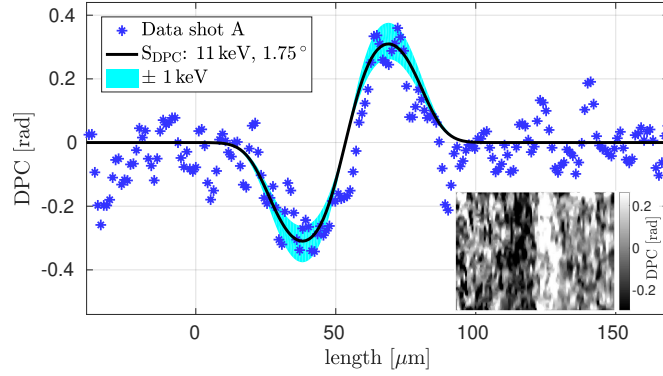


**Figure 4.** The differential phase-contrast DPC reconstructed for shot A. The measured data (points) is averaged over 80 lines across the polyimide foil. It is overlaid by the calculated signal  $S_{DPC}$  (solid line), which is calculated for 11 keV with a tilt angle of  $1.75^\circ$ . The band (light blue) indicates the calculated DPC signal for the  $\pm 1$  keV uncertainty of the x-ray energy. The inset shows the reconstructed DPC image of the full object region of interest. The foil shows the typical dark-and-bright signature of a differential phase-contrast image. Image noise is reduced with a median filter.

differential phase corresponds to increasing thickness of the object while positive values indicate that the object becomes thinner.

The phase-signal shown in figure 4 is calculated for mono-energetic x-rays. Concerning the object geometry, the only free parameter is the angle by which the foil is tilted. A larger tilt angle corresponds to a wider DPC signal and a slower rise of the edges of the object thickness profile. This means the differential phase becomes weaker with larger tilt angles. The differential phase is also influenced by the x-ray energy. A higher energy means a smaller differential phase because the decrement  $\delta$  of the polyimide foil decreases. To find the best parameters for the calculation, the energy was varied in 0.5 keV steps and the tilt angle in  $0.05^\circ$  steps in a range from  $0^\circ$  to  $2^\circ$ . The error margin is given as twice the step size. Best agreement between the calculated and measured data was found for a tilt angle of  $1.75^\circ \pm 0.1^\circ$  and an x-ray energy of  $11 \text{ keV} \pm 1 \text{ keV}$  for shot A. At these parameter values, the mean square deviation between the measurement data and the calculation is minimal.

### 3.2 Reconstruction of the transmission

The reconstructed transmission image taken with shot A is shown in the inset in figure 5. The foil is visible as a dark stripe in the centre. The asymmetric, bright boundaries around the stripe are the in-line phase-contrast signatures due to wave propagation, that can also be observed in the raw image in figure 1. The measured transmission data in figure 5 is averaged over 80 lines of the region of interest. The absorption in the foil can be seen as negative peak in the central region of the transmission profile. The deformation of this peak and the two positive peaks at the boundaries are caused by wave propagation effects.

The phase-contrast image could be retrieved by analysing the in-line signatures [1–6, 40]. However, we already reconstructed the object with the grating-based approach. So, instead of reconstructing it again (with an in-line method), the object properties are used to calculate the

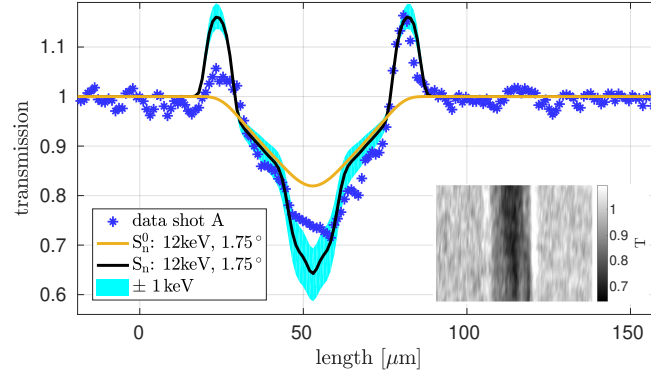


**Figure 5.** Reconstructed transmission  $T$  plotted for shot A. The measured data (points) is averaged over 80 lines across the polyimide foil. It is overlaid by two calculated curves. The calculated signal  $S_n^0$  neglects the effects of the wave propagation between the sample and the detector.  $S_n$  includes propagation effects, leading to distinct in-line phase-shift signatures. Both calculations assume a mono-energetic radiation of 12 keV and a tilt angle of  $1.75^\circ$ . The inset shows the transmission image of the full region of interest. As can be seen, the moiré fringes are successfully removed via the Fourier analysis of the image data.

expected in-line signatures in the detector plane. From this, a good consistency between the so calculated signal and the measured transmission data is expected.

The in-line signatures are calculated using the same tilt angle that was found by the grating-based phase-reconstruction. However as outlined above, a small difference in energy is expected due to the energy-dependence of the moiré visibility (see figure 3). So, the energy is optimised separately for the transmission data. Again, the mean square deviation is used to quantify the agreement between calculation and measured data. The measured data shows an asymmetry between the in-line signatures on the left and the right side of the object. This is not reproduced in the calculation because the object is approximated by a symmetric trapezoidal density profile. The asymmetric peaks at the boundaries are problematic for the optimisation. So, the narrow peaks are neglected and the optimisation regards only the central region of the polyimide foil. For the transmission signature of shot A, best agreement was found at 12 keV, which is 1 keV above the result for the phase reconstruction. The corresponding calculated transmission  $S_n$  is plotted in figure 5.

Although there is still a deviation between the calculated transmission and the measured data, the in-line features are reproduced at least qualitatively. For comparison, the signal  $S_n^0$  is calculated with the same parameters, but neglects the propagation effects that lead to the in-line signatures. It is plotted in figure 5 as well. It demonstrates, that taking propagation effects into account is essential for the understanding of our imaging setup.

### 3.3 Check of the reproducibility of the results

The analysis of shot A was then repeated for two more shots (shot B and C) which were recorded with the same imaging setup, laser parameters and reference image. The results are plotted in figure 6. We obtained different tilt angles for each shot, which is expected since the polyimide foil is

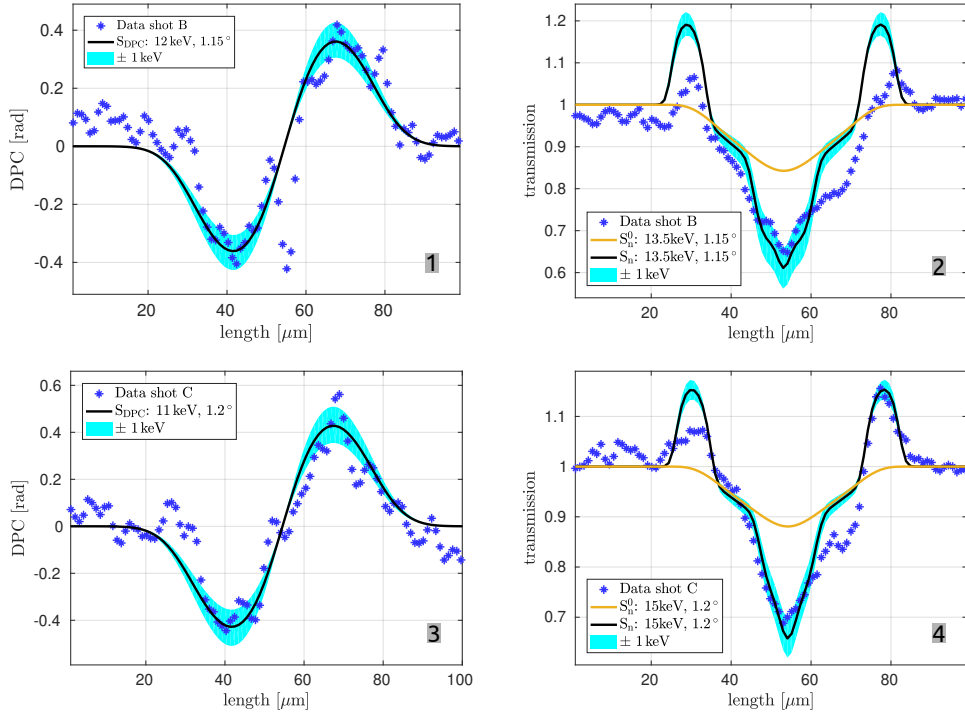


**Figure 6.** Reconstructed images of shot B (1 and 2) and C (3 and 4) for the DPC (1 and 3) and the transmission (2 and 4). The calculated signals of the DPC  $S_{\text{DPC}}$ , the transmission with phase-effects  $S_n$  and the transmission without phase-effects  $S_n^0$  are plotted for the optimised parameters. The band (light blue) gives the  $\pm 1$  keV uncertainty.

replaced after every shot. Also, the determined energies vary which we attribute to the shot-to-shot variations in the laser power and the resulting x-ray spectra.

The determined energies lie between 11 keV and 12 keV for the grating-based phase-images and between 12 keV and 15 keV for the transmission images. This is in agreement with the mean energy reported by Seifert et al. [38]. For all three shots, the determined energy for the transmission image is higher than for the DPC. The ratio between the determined energies is not constant, with the smallest difference in shot A, where the energies are 11 keV and 12 keV. The largest difference is found for shot C with 11 keV and 15 keV for the DPC and transmission respectively. As the visibility of our setup (see figure 3) is quite significantly selective to the x-ray spectrum in the region of 5 keV to 20 keV for the phase-image, the shot-to-shot variation in the spectrum can induce larger changes in the effective energy of the transmission image compared to the phase-image.

The tilt angles vary between  $1.15^\circ$  and  $1.75^\circ$  which is consistent with our estimations of the mechanical reliability of the object-mount. For the three transmission curves, the minima lie between 60% and 75% transmission. The three phase-signals show amplitudes from minus-peak to plus-peak from 0.6 rad to 1.0 rad. Concerning the transmission signals, propagation effects cannot be neglected for a quantitative analysis in our imaging setup. The in-line signatures are asymmetric, but very distinct. For the shots A and C even the calculated signal  $S_n$ , which also regards the propagation effects, can only reproduce a part of the measured transmission. This demonstrates

that the very simple model is suited only for a rough quantitative interpretation of the transmission images. Qualitatively, the in-line signatures are mostly reproduced by the calculations for all three shots. For the phase-images, good agreement between measurement data and calculation was found within the  $\pm 1$  keV-band for all three shots. The comparison of the three shots shows that the results are reproducible.

## 4 Conclusion and outlook

Images of a 25  $\mu\text{m}$  wide and 1 mm thick, slightly tilted polyimide foil with a 47-fold image magnification are presented. They were successfully reconstructed for the differential phase-contrast yielding reproducible results. The calculations for the phase-images are quantitatively in fairly good agreement with the data. In-line signatures are prominent in the transmission images. The provided calculations show, that these signatures are plausible for the geometry of the setup and the test objects. This shows that grating-based phase-contrast imaging is possible with a laser-driven backlighter at the PHELIX facility at the GSI Helmholtzzentrum für Schwerionenforschung GmbH, by using a rigid portable two grating setup and a fast alignment method.

Future experiments might require adjustments of the imaging setup. For example a higher phase-sensitivity can be achieved by bringing the G1 closer to the sample and thereby reducing the magnification  $M_{G1}$  from the object into the G1 plane [42]. Smaller grating periods increase the phase-sensitivity as well but pose a challenge for the production of the gratings. An object with finer details requires a higher detector resolution or larger image magnification which can be adjusted by the geometry of the setup. In that way, the results of this work can be used as a benchmark for future experiments.

## Acknowledgments

The results presented here are based on the experiment P186, which was performed at the PHELIX facility at the GSI Helmholtzzentrum für Schwerionenforschung, Darmstadt (Germany) in the frame of FAIR Phase-0. We would like to give a special thanks to the PHELIX operation team. Further we would like to thank Hennry Schott (ECAP) for his technical support. The authors acknowledge the support of the Karlsruhe Nano Micro Facility (KNMF), a Helmholtz Research Infrastructure at Karlsruhe Institute of Technology, and microworks GmbH for fabricating the gratings.

## References

- [1] D. Chapman et al., *Diffraction enhanced x-ray imaging*, *Phys. Med. Biol.* **42** (1997) 2015.
- [2] A. Snigirev, I. Snigireva, V. Kohn, S. Kuznetsov and I. Schelokov, *On the possibilities of x-ray phase contrast microimaging by coherent high-energy synchrotron radiation*, *Rev. Sci. Instrum.* **66** (1995) 5486
- [3] T.J. Davis, D. Gao, T.E. Gureyev, A.W. Stevenson and S.W. Wilkins, *Phase-contrast imaging of weakly absorbing materials using hard x-rays*, *Nature* **373** (1995) 595.
- [4] P. Cloetens, R. Barrett, J. Baruchel, J.P. Guigay and M. Schlenker, *Phase objects in synchrotron radiation hard x-ray imaging*, *J. Phys. D* **29** (1996) 133.

- [5] R. Toth et al., *Evaluation of ultrafast laser-based hard x-ray sources for phase-contrast imaging*, *Phys. Plasmas* **14** (2007) 053506.
- [6] A. Scropp et al., *Imaging shock waves in diamond with both high temporal and spatial resolution at an xfel*, *Sci. Rept.* **5** (2015) 11089.
- [7] U. Bonse and M. Hart, *An x-ray interferometer*, *Appl. Phys. Lett.* **6** (1965) 155.
- [8] A. Momose, *Demonstration of phase-contrast x-ray computed tomography using an x-ray interferometer*, *Nucl. Instrum. Meth. A* **352** (1995) 622.
- [9] A. Olivo et al., *An innovative digital imaging set-up allowing a low-dose approach to phase contrast applications in the medical field*, *Med. Phys.* **28** (2001) 1610.
- [10] A. Olivo and R. Speller, *A coded-aperture technique allowing x-ray phase contrast imaging with conventional sources*, *Appl. Phys. Lett.* **91** (2007) 074106.
- [11] C. David, B. Nöhammer, H.H. Solak and E. Ziegler, *Differential x-ray phase contrast imaging using a shearing interferometer*, *Appl. Phys. Lett.* **81** (2002) 3287.
- [12] A. Momose et al., *Demonstration of X-Ray Talbot Interferometry*, *Japn. J. Appl. Phys.* **42** (2003) L866.
- [13] T. Weitkamp et al., *X-ray phase imaging with a grating interferometer*, *Opt. Express* **13** (2005) 6296.
- [14] F. Pfeiffer, T. Weitkamp, O. Bunk and C. David, *Phase retrieval and differential phase-contrast imaging with low-brilliance x-ray sources*, *Nature Phys.* **2** (2006) 258.
- [15] T. Michel et al., *On a dark-field signal generated by micrometer-sized calcifications in phase-contrast mammography*, *Phys. Med. Biol.* **58** (2013) 2713.
- [16] F. Pfeiffer et al., *Hard-x-ray dark-field imaging using a grating interferometer*, *Nature materials* **7** (2008) 134.
- [17] S. Bachche et al., *Laboratory-based x-ray phase-imaging scanner using talbot-lau interferometer for non-destructive testing*, *Sci. Rept.* (2017) 6711.
- [18] V. Ludwig et al., *Non-destructive testing of archaeological findings by grating-based x-ray phase-contrast and dark-field imaging*, *J. Imaging* **4** (2018) 58.
- [19] V. Ludwig et al., *A phase-sampling method for an x-ray talbot-lau scanner with continuous grating movement*, *2020 JINST* **15** P01010.
- [20] D. Ress et al., *Measurement of laser-plasma electron density with a soft x-ray laser deflectometer*, *Science* **265** (1994) 514.
- [21] D. Stutman, M.P. Valdivia and M. Finkenthal, *X-ray moiré deflectometry using synthetic reference images*, *Appl. Opt.* **54** (2015) 5956.
- [22] M.P. Valdivia et al., *An x-ray backlit talbot-lau deflectometer for high-energy-density electron density diagnostics*, *Rev. Sci. Instrum.* **87** (2016) 023505.
- [23] V. Bouffetier et al., *Proof-of-concept Talbot-Lau x-ray interferometry with a high-intensity, high-repetition-rate, laser-driven k-alpha source*, *Appl. Opt.* **59** (2020) 8380.
- [24] M.P. Valdivia et al., *Implementation of a Talbot-Lau x-ray deflectometer diagnostic platform for the OMEGA EP laser*, *Rev. Sci. Instrum.* **91** (2020) 023511.
- [25] F. Barbato et al., *Propagation-based imaging phase-contrast enhanced imaging setup for single shot acquisition using laser-generated x-ray sources*, *2019 JINST* **14** C03005.
- [26] L. Antonelli et al., *X-ray phase-contrast imaging for laser-induced shock waves*, *EPL* **125** (2019) 35002.

- [27] M. Schuster et al., *A fast alignment method for grating-based x-ray phase-contrast imaging systems*, [2019 JINST 14 P08003](#).
- [28] L. Antonelli et al., *Laser-driven shock waves studied by x-ray radiography*, [Phys. Rev. E 95 \(2017\) 063205](#).
- [29] V. Arrizón and E. López-Olazagasti, *Binary phase grating for array generation at 1/16 of talbot length*, [J. Opt. Soc. Amer. A 12 \(1995\) 801](#).
- [30] T.J. Suleski, *Generation of lohmann images from binary-phase talbot array illuminators*, [Appl. Opt. 36 \(1997\) 4686](#).
- [31] M. Takeda, H. Ina and S. Kobayashi, *Fourier-transform method of fringe-pattern analysis for computer-based topography and interferometry*, [J. Opt. Soc. Am. 72 \(1982\) 156](#).
- [32] W. Yashiro, Y. Terui, K. Kawabata and A. Momose, *On the origin of visibility contrast in x-ray talbot interferometry*, [Opt. Express 18 \(2010\) 16890](#).
- [33] V. Bagnoud et al., *Commissioning and early experiments of the phelix facility*, [Appl. Phys. B 100 \(2010\) 137](#).
- [34] B. Borm, D. Khaghani and P. Neumayer, *Properties of laser-driven hard x-ray sources over a wide range of laser intensities*, [Phys. Plasmas 26 \(2019\) 023109](#).
- [35] G. Fiksel, F.J. Marshall, C. Mileham and C. Stoeckl, *Note: spatial resolution of Fuji BAS-TR and BAS-SR imaging plates*, [Rev. Sci. Instrum. 83 \(2012\) 086103](#).
- [36] P. Meyer, J. Schulz and V. Saile, *Deep x-ray lithography*, in [Micromanufacturing Engineering and Technology](#), 1<sup>st</sup> edition, Yi Qin ed., William Andrew Publishing, U.S.A. (2010).
- [37] P. Meyer and J. Schulz, *Deep x-ray lithography*, in [Micromanufacturing Engineering and Technology](#), 2<sup>nd</sup> edition, Yi Qin ed., William Andrew Publishing, U.S.A. (2010).
- [38] M. Seifert et al., *Evaluation of the weighted mean x-ray energy for an imaging system via propagation-based phase-contrast imaging*, [J. Imaging 6 \(2020\) 63](#).
- [39] B. Henke, E. Gullikson and J. Davis, *X-ray interactions: Photoabsorption, scattering, transmission, and reflection at  $e = 50\text{--}30,000$  eV,  $z = 1\text{--}92$* , [Atomic Data and Nuclear Data Tables 54 \(1993\) 181](#).
- [40] D.M. Paganin, *Coherent x-ray optics*, Oxford University Press, Oxford U.K. (2006).
- [41] M. Engelhardt et al., *High-resolution differential phase contrast imaging using a magnifying projection geometry with a microfocus x-ray source*, [Appl. Phys. Lett. 90 \(2007\) 224101](#).
- [42] T. Donath et al., *Inverse geometry for grating-based x-ray phase-contrast imaging*, [J. Appl. Phys. 106 \(2009\) 054703](#).